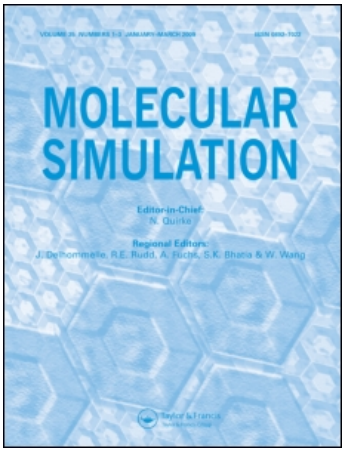

Molecular Simulation
Publication details, including instructions for authors and subscription information:
http://www.informaworld.com/smpp/title~content=t713644482

Molecular Dynamics Simulation of the Fast Ion Conductor δ-Bi_2O_3. II. Sub-lattice Structure

D. A. Mac Dónaill[ab]; P. W. M. Jacobs[c]; Z. A. Rycerz[c]
[a] Department of Chemistry, Trinity College, Dublin 2, Republic of Ireland [b] Central Research Laboratory, Hitachi Ltd., Tokyo, Japan [c] Department of Chemistry, The University of Western Ontario, London, Ontario, Canada

To cite this Article Dónaill, D. A. Mac , Jacobs, P. W. M. and Rycerz, Z. A.(1990) 'Molecular Dynamics Simulation of the Fast Ion Conductor δ-Bi_2O_3. II. Sub-lattice Structure', Molecular Simulation, 5: 3, 193 — 214
To link to this Article: DOI: 10.1080/08927029008022131
URL: http://dx.doi.org/10.1080/08927029008022131

Molecular Simulation, 1990, Vol. 5, pp. 193–214
Reprints available directly from the publisher
Photocopying permitted by license only

MOLECULAR DYNAMICS SIMULATION OF THE FAST ION CONDUCTOR δ-Bi_2O_3. II. SUB-LATTICE STRUCTURE

D.A. MACDÓNAILL,†

Department of Chemistry, Trinity College, Dublin 2, Republic of Ireland

P.W.M. JACOBS* and Z.A. RYCERZ,

Department of Chemistry, The University of Western Ontario, London, Ontario, Canada N6A 5B7

(*Received October 1989, accepted December 1989*)

The results of molecular dynamics (MD) simulations of δ-Bi_2O_3 are analyzed with a view to obtaining an increased understanding of the structure of the Bi^{3+} and O^{2-} sub-lattices. The existence of cube-edge O^{2-} interstitials and of Willis-like disorder is confirmed by density maps. The onset of fast-ion conduction is associated with changes in the structure of both sub-lattices. Interpretation of the results suggests the existence of more than one fluorite form, differing in the structure of the O^{2-} sublattice.

KEY WORDS: Bismuth oxide, bismuth sesquioxide, fluorite, molecular dynamics, fast-ion conduction.

1. INTRODUCTION

In this second paper of the series we examine the structure of the Bi^{3+} and O^{2-} sub-lattices in the fast ion conductor δ-Bi_2O_3 through calculations of the ionic positions as functions of time. These are displayed as projections of the contents of the simulation box, and of the ionic densities, both in particular planes and along certain high-symmetry directions in various planes. To aid interpretation of these, the Sillen model for δ-Bi_2O_3 is depicted in Figure 1. Simulation conditions and details of the potentials were reported in paper I [1] of this series and so we review these here only briefly, in order to make this paper self-contained.

The four MD simulations of δ-Bi_2O_3 were performed under conditions of constant volume using the rigid-ion approximation. The simulation box contained a cubic $3 \times 3 \times 3$ array of Bi_4O_6 pseudo-flourite cells, giving a total of 270 particles. A time-step of $\Delta t = 5 \times 10^{-15}$s was employed, and positions and velocities were recorded for more than 2000 time steps after equilibration.

Two sets of conditions were used [1]. In the first, set I, termed "experimental conditions", the calculations were performed using the lattice constant and temperature at which fast-ion conduction is observed to occur experimentally (see Table

† Currently at Central Research Laboratory, Hitachi Ltd., P.O. Box 2, Kokubunji, Tokyo 185, Japan.
* Associated with the Centre for Interdisciplinary Studies in Chemical Physics, The University of Western Ontario.

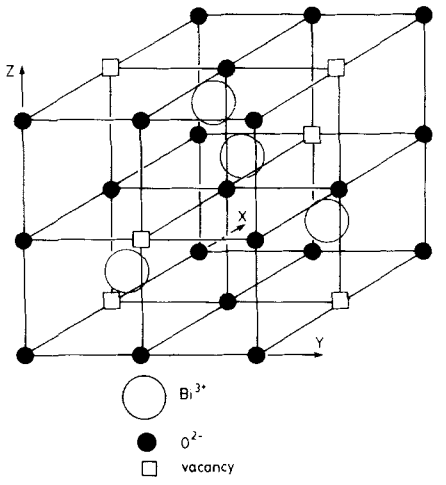

Figure 1 Unit cell of δ-Bi_2O_3 containing Bi_4O_6. In the Sillen structure shown, O^{2-} vacancies are ordered along $<111>$.

1). However, none of the simulations exhibited fast-ion conduction under these conditions. Accordingly, a second set of simulations, set II, were performed under what we refer to as "relaxed conditions", with elevated temperatures up to almost 1600 K and appropriately expanded lattice constants (Tables 1 and 2 in [1]). For reasons outlined below we will concentrate here on the simulations with $T = 1500$ K. These rather extreme conditions were intended to compensate for the artificial constraints imposed by constant volume and periodic boundary conditions (cf. [2]).

Table 1 Simulation conditions: I, II indicate 'experimental' and 'relaxed' conditions; *R*, *D* denote rigid-ion or dielectrically adjusted potential

Simulation	*Lattice Constant (Å)*	*Equilibrated Temperature (K)*	*Figure Reference**
I-*R*1	5.644	1017	a
I-*D*1	5.644	1026	b
II-*R*2-2	5.721	1489	c
II-*D*2-2	5.721	1489	d

*Figure sections a, b, c, d of Figures 2–15 are as indicated in this table, except for Figure 11 which has two extra sections and Figure 12 which has one. Differences are explained in the captions. Figure 16 does not adhere to this pattern and the two parts of Figure 16 are captioned individually.

Table 2 Observed and calculated O^{2-} displacements in pure and yttria doped Bi_2O_3

		<111> interstitials	*<100> interstitials*
Battle *et al.* [7,8]			
pure Bi_2O_3	1023 K	1.02 Å	—
27% doped Bi_2O_3	1023 K	0.68 Å	—
27% doped Bi_2O_3	298 K	0.65 Å	—
Infante *et al.* [9]			
25% doped Bi_2O_3	298 K	0.80 Å	0.335 Å
this work			
pure Bi_2O_3		0.77 ± 0.15 Å*	0.27 ± 0.09 Å*

*See Appendix

Two sets of potentials were used [1]. The first set was based on modified electron gas (MEG) potentials fitted, using the shell model of ionic polarizability, to experimental data and with no adjustments made to compensate for the absence of polarizability necessitated by the rigid-ion model employed here. This potential set is identified by the letter *R*. These potentials, together with potentials with some measure of ionic polarizability, have proved very useful in static lattice calculations on δ-Bi_2O_3 [3].

In the second set of potentials, denoted *D* (for dielectrically adjusted), the short-range Bi^{3+}-O^{2-} potential was adjusted to fit the static dielectric constant; the second-neighbour potentials were not changed. The combination of two sets of potentials with two sets of simulation conditions gave a total of four simulations for which the data were analyzed. For both the *D* and *R* potential sets, there is a slight difference in the Bi^{3+}-O^{2-} potential used under 'experimental' and 'relaxed' conditions. The simulations under 'experimental' conditions, being performed first, were run using Bi^{3+}-O^{2-} potentials fitted to the high-temperature experimental lattice constant of 5.644 Å; recently we have obtained a reliable room-temperature lattice of δ-Bi_2O_3, leading to consistent thermal expansivity and consequently a 0 K lattice constant [4], to which both the *R* & *D* Bi^{3+}-O^{2-} potentials were refitted. Only the σ hardness parameter (Table 1 in [1]) needed to be adjusted and the changes required were slight and not very significant. Consequently, the potential sets used under 'experimental' conditions are designated *R*1 and *D*1, while those used under 'relaxed' conditions are referred to as *R*2 and *D*2. A number of other simulations, with appropriate lattice constants were performed under relaxed conditions at approximately 1300 K (II-*R*2-1, II-*D*2-1) and 1600 K (II-*R*2-3, II-*D*2 3). However, the simulations at 1300 K and 1600 K either failed to exhibit fast-ion conduction or a phase change occurred, so that for the relaxed simulation we concentrate here on the two simulations at 1500 K. For paper I we recorded that we had found it necessary to use both dielectrically adjusted potentials (*D*) and relaxed conditions (II) for fast-ion conduction to occur, the evidence for this being obtained from projections of the O^{2-} sub-lattice in the simulation box and from histograms of O^{2-} ion displacements [1]. In this paper we examine each sub-lattice in turn in considerable detail, with a view to understanding the nature of fast-ion conduction in δ-Bi_2O_3.

2. THE BISMUTH SUB-LATTICE

Simulation I-*R*1, under experimental conditions, yields a crystalline, system. Over the whole simulation of 2000 time steps, only a single O^{2-} jump occurred [1]. The Bi^{3+} sub-lattice is, as one might therefore expect, highly ordered. The Bi^{3+}-Bi^{3+} radial distribution function $g(r)$ in Figure 2a exhibits four clearly defined peaks: note the splitting of the first peak due to Bi^{3+}-Bi^{3+} nearest-neighbours (*nn*). The splitting is indicative of significant displacements of Bi^{3+}'s from the perfect lattice positions. This is clearly seen in the simulation box projection for simulation I-*R*1 (Figure 3a). Static lattice simulations [3] found that the Bi^{3+} displacement readily occurred in response to a change in structure in the O^{2-} sub-lattice. The splitting largely disappears with the dielectrically adjusted potential, run I-*D*1 (Figure 2b), but little else changes. For II-*R*2-2 (Figure 2c) the peaks are broadened, that due to forth neighbours (4*n*) being flattened substantially. In II-*D*2-2, for the dielectrically adjusted potential under relaxed conditions (Figure 2d) all the peaks are considerably broadened and flattened,

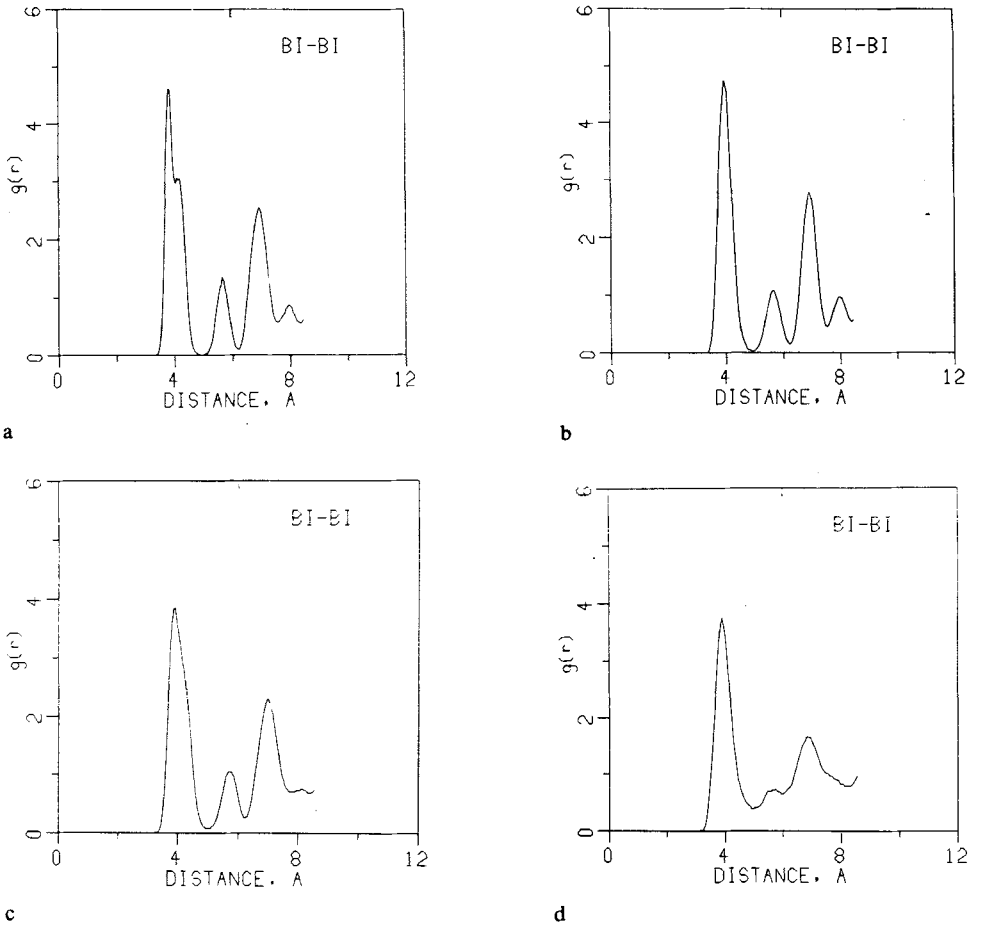

Figure 2 Radial distribution function for Bi^{3+}-Bi^{2+}. The same designations (a) I-*R*1; (b) I-*D*1; (c) II-*R*2-2; (d) II-*D*2-2 are followed in all the figures except Figures 11, 12 and 16, and this designation is included in Table 1 for ready-reference.

the 2*n* and 4*n* peaks being most noticeably reduced. [N.B. With three exceptions, and unless otherwise specified, the same sequence (a) I-*R*1, (b) I-*D*1, (c) II-*R*2-2 (d) II-*D*2-2 is followed for each of the figures. Table 1 provides a ready reference].

Projections of the Bi^{3+} sub-lattice emphasize this situation. For I-*R*1 Figure 3a shows a clearly crystalline sub-lattice with some evidence of a 3-fold screw axis. Dielectric adjustment I-*D*1, or relaxed conditions II-*R*2-2, both induce increased vibrational motion (Figures 3b, 3c) and this is most marked with both features are present as in II-*D*2-2 (Figure 3d). The effects may be synergistic for, as plots of Bi^{3+} density in the (400) and (220) planes show (Figure 4,5) dielectric adjustment does not have a great effect at 1026 K (Figures 4b, 5b) while increased temperature induces some broadening in the density distribution (Figures 4c, 5c) but the combination of both gives a much broader and flatter distribution with some multiplet structure (Figures 4d, 5d).

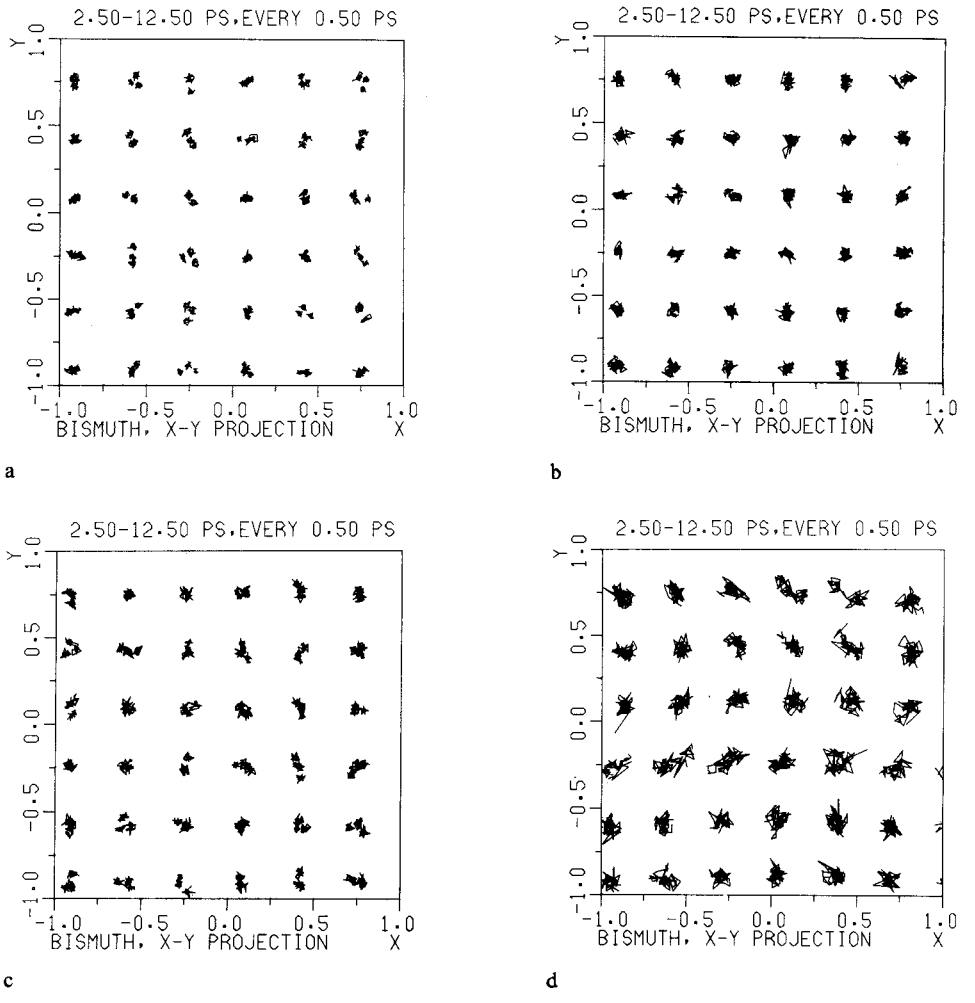

Figure 3 Projections of the contents of the simulation box in the *XY* plane showing the successive positions of the Bi^{3+} atoms at 0.50 ps intervals over a period of 10 ps.

The effects of the changes in potentials and lattice constant are illustrated even more clearly by plots of density distributions along the principal directions in the cubic lattice, namely <100>, <110> and <111> (Figures 6,7,8). Along all these three directions the peaks for I-*D*1 appear sharper than for I-*R*1. This might seem strange at first because of the greater ampliturde of the Bi^{3+} vibrations with I-*D*1 (contrast Figures 3a, 3b). However, it is the displacement of the Bi^{3+} ions from their lattice sites in I-*R*1 (Figure 3a) which gives a broader density distribution in Figures 6a, 7a, 8a, despite a smaller vibrational amplitude.) The smaller displacements in I-*D*1 are responsible for the loss of the doublet structure of the first peak in $g(r)$ for I-*D*1 (Figure 2b), where the *nn* maximum lies between the two maxima of the *nn* doublet in I-*R*1 (Figure 2a). In II-R2-2 the arrangement of Bi^{3+} ions has become even more

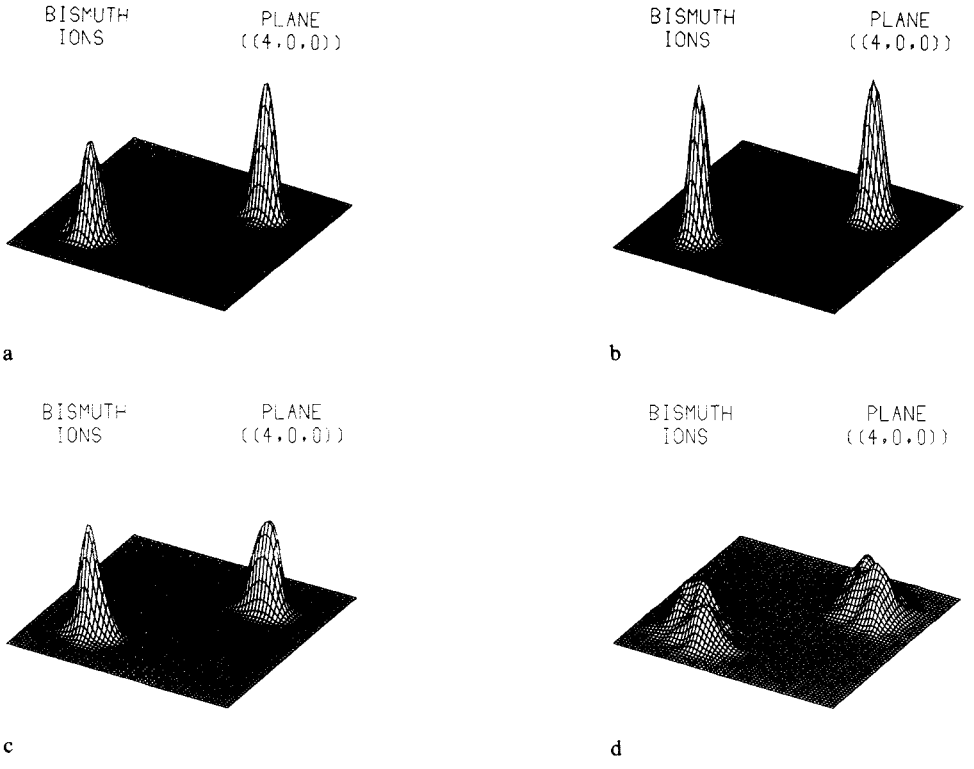

Figure 4 3-D plot of the Bi^{3+} density in a thin slice (1/32 of the lattice constant in thickness) containing the (400) plane. For brevity and convenience, this is referred to as the Bi^{3+} density in the (400) plane. Note that the density of (d) is multiplied by a factor of 3.33 compared to (a), (b) and (c).

disordered through increased Bi^{3+} vibrations (Figure 3c), so that the doublet structure of the *nn* peak in $g(r)$ has all but dissappeared (Figure 2c), remaining only as a slight shoulder, and the density distributions are of reduced height (Figures 6c, 7c, 8c). For II-*D*2-2, however, the extraordinary flattening and broadening of the Bi^{3+} density peaks is clearly evident in Figures 6d,7d,8d. [Notice the scale change of a factor of 10 in the ordinates of (d) compared to (a), (b) and (c) in this sequence of figures.]

3. THE OXYGEN SUB-LATTICE

Only in simulation II-*D*2-2 was fast-ion conduction observed in the projections of ion positions and histograms of O^{2-} displacements (see Figures 1,2,3 of part I [1]). One would therefore expect to see evidence of increased disorder in the O^{2-} sub-lattice (II-*D*2-2) and this is precisely what is observed. In $g(r)$ for Bi^{3+}-O^{2-}, shown in Figure 9, both I-*D*1 (Figure 9b) and II-*R*2-2 (Figure 9c) show some broadening with respect to I-*R*1, but this is considerably less than II-*D*2-2 (Figure 9d), where only the *nn* and 2*n* peaks remain clearly resolved. The adjustment in potentials to match the static dielectric constant (I-*D*1) introduces greater fluidity in the O^{2-} sub-lattice and

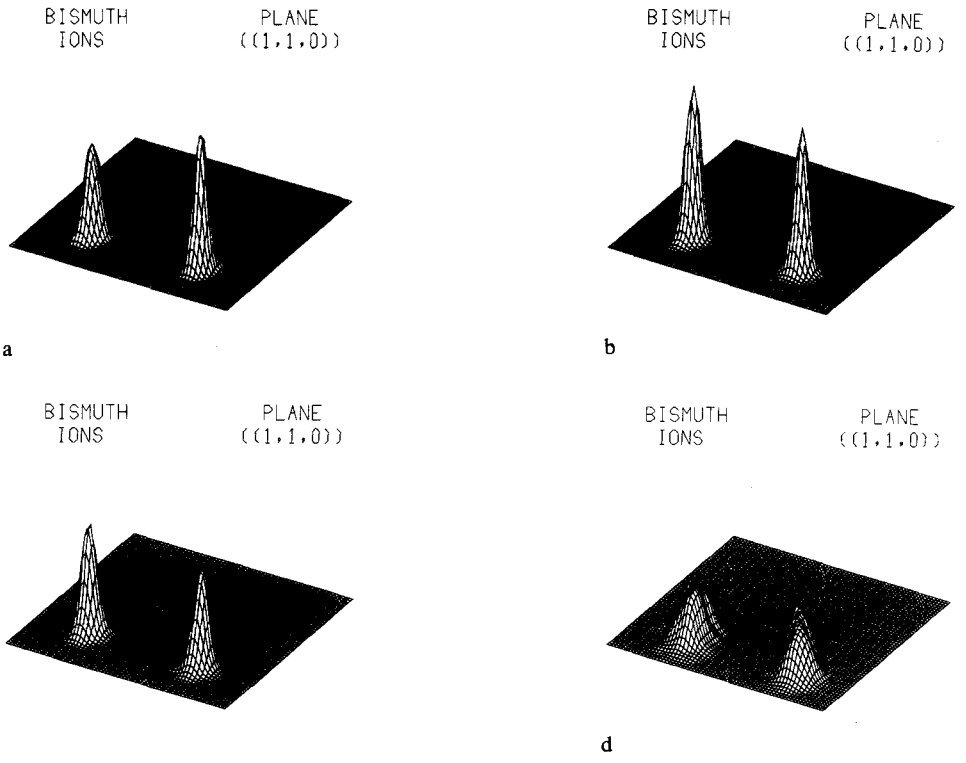

Figure 5 3-D plot of the Bi^{3+} density in the (110) plane. Note that the density of (d) is multiplied by a factor of 3.33 compared to (a), (b) and (c).

therefore greater broadening of the peaks in $g(r)$ for O^{2-}-O^{2-} (Figure 10b) than does the relaxation of the lattice and increased temperature (II-*R*2-2 in Figure 10c) although the latter case, as expected, demonstrates greater vibrational disorder than I-*R*1 (Figure 10a). In II-*D*2-2 (Figure 10d), with both an adjusted potential and relaxed conditions, further broadening of the peaks in the O^{2-}-O^{2-} $g(r)$ occurs so that only the *nn* and 4*n* peaks can still be identified clearly. In II-*D*2-2 the O^{2-} sub-lattice thus appears to be much more liquid-like than in the other three simulations, which is entirely consistent with the observation of fast-ion conduction in this simulation alone.

The structure of the Bi^{3+} sub-lattice is affected slightly more by relaxed conditions than by the $R \rightarrow D$ adjustment of the potential as can be seen in $g(r)$ for Bi^{3+}-Bi^{3+} (Figure 2) and the Bi^{3+} density distributions displayed in Figures 6,7,8. This behaviour is hardly surprising since the absence of ionic polarizability in the rigid-ion model was compensated for by dielectric adjustment of the Bi^{3+}-O^{2-} pair potential. This ought to affect not only $g(r)$ for Bi^{3+}-O^{2-}, but that of O^2-O^{2-} also, since O^{2-} is the more mobile species. The Bi^{3+}-Bi^{3+} distribution is only indirectly affected by this adjustment. By contrast with Bi^{3+}, the O^{2-} sub-lattice is changed more by the dielectric adjustment of the potential than it is by increased temperature and lattice expansion, as can be seen from the broadening of the peaks in $g(r)$ for Bi^{3+}-O^{2-} and

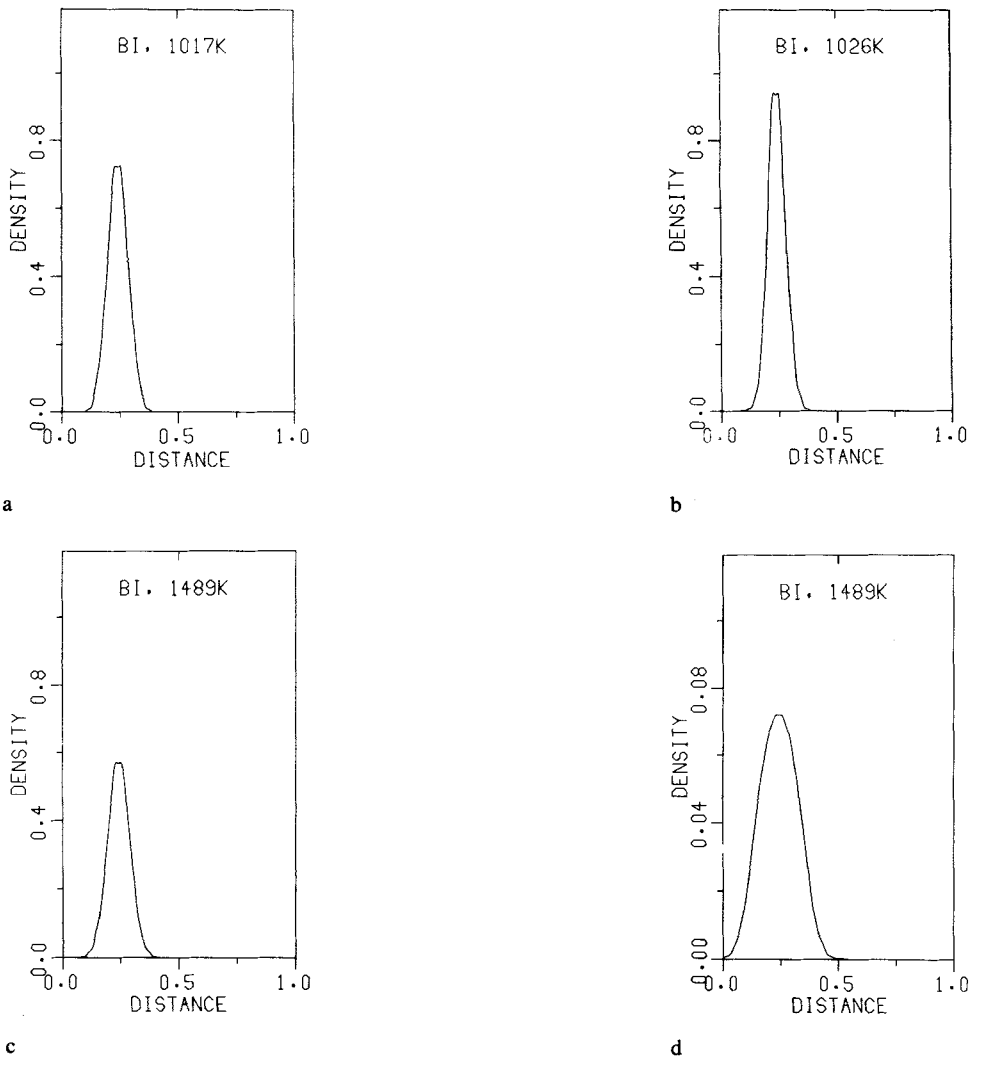

Figure 6 Bi^{3+} density averaged over equivalent $<100>$ directions. Distance in units of the lattice parameter a. Density units are: number of ions/grid element/time step. Size of grid element = $a/32$.

O^{2-}-O^{2-} (Figures 9, 10 compare Figures 9b and 10b with 9c and 10c). It is also apparent in the 3-D density plots for O^{2-} in the (100) plane (Figure 11). The peaks in Figures 11a, 11c for II-*R*1 and II-*R*2-2 are sharper and those for II-*D*1 (Figure 11b); in all three cases the O^{2-} density between the peaks falls to zero along $<100>$ directions. In the fast-ion conducting simulation, II-*D*2-2 (Figure 11d), the density at O^{2-} lattice sites is reduced considerably, the maxima decreasing by a factor of 10 (note the expanded scale). These peaks now show a multiplet character (Figure 11d) which is particularly evident at the corners. Moreover, the O^{2-} density along $<100>$ no longer falls to zero. The multiplet character strongly suggests the presence of significant O^{2-} density displaced along $<100>$ directions.

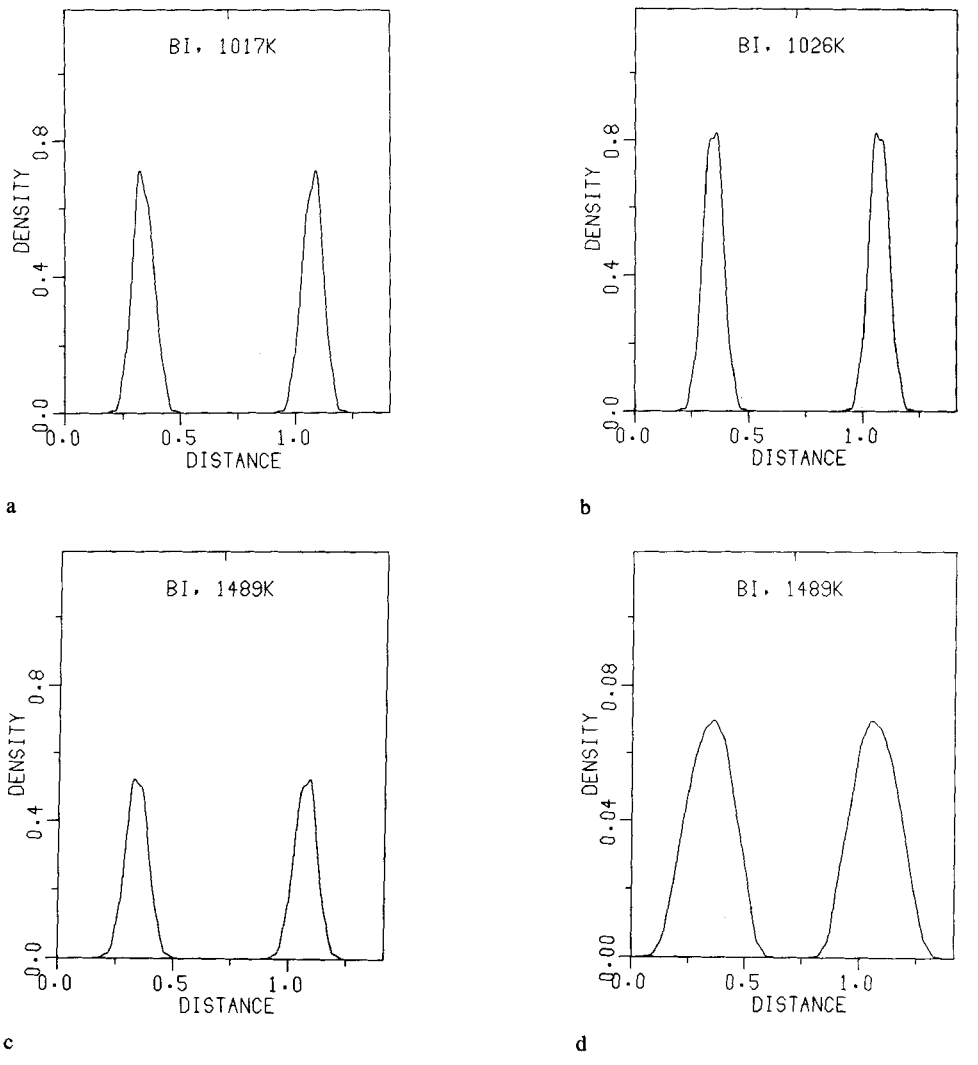

Figure 7 Bi^{3+} density along <110>. Units as in Figure 6 but with a grid element size of $\sqrt{2}a/32$.

O^{2-} densities were determined by averaging over all 27 Bi_4O_6 cells in the simulation box and further averaging based on the assumption that each cell possessed cubic symmetry. However, in the plots shown (Figures 11,12) the densities in the (100) and (200) O^{2-} planes were deliberately not averaged (although these planes ought to be equivalent) in order than the existence of lower symmetry structures, namely differences in the O^{2-} density distribution, might emerge if present, and not be obscured by overzealous averaging. In the (200) plane (Figure 11e) the O^{2-} distribution differs in its detail from the (100) plane. O^{2-} density maxima displaced along <110> directions may clearly be seen as shoulders in the edge peaks. These shoulders along <110> directions could be caused by either <110> or <111> displacements.

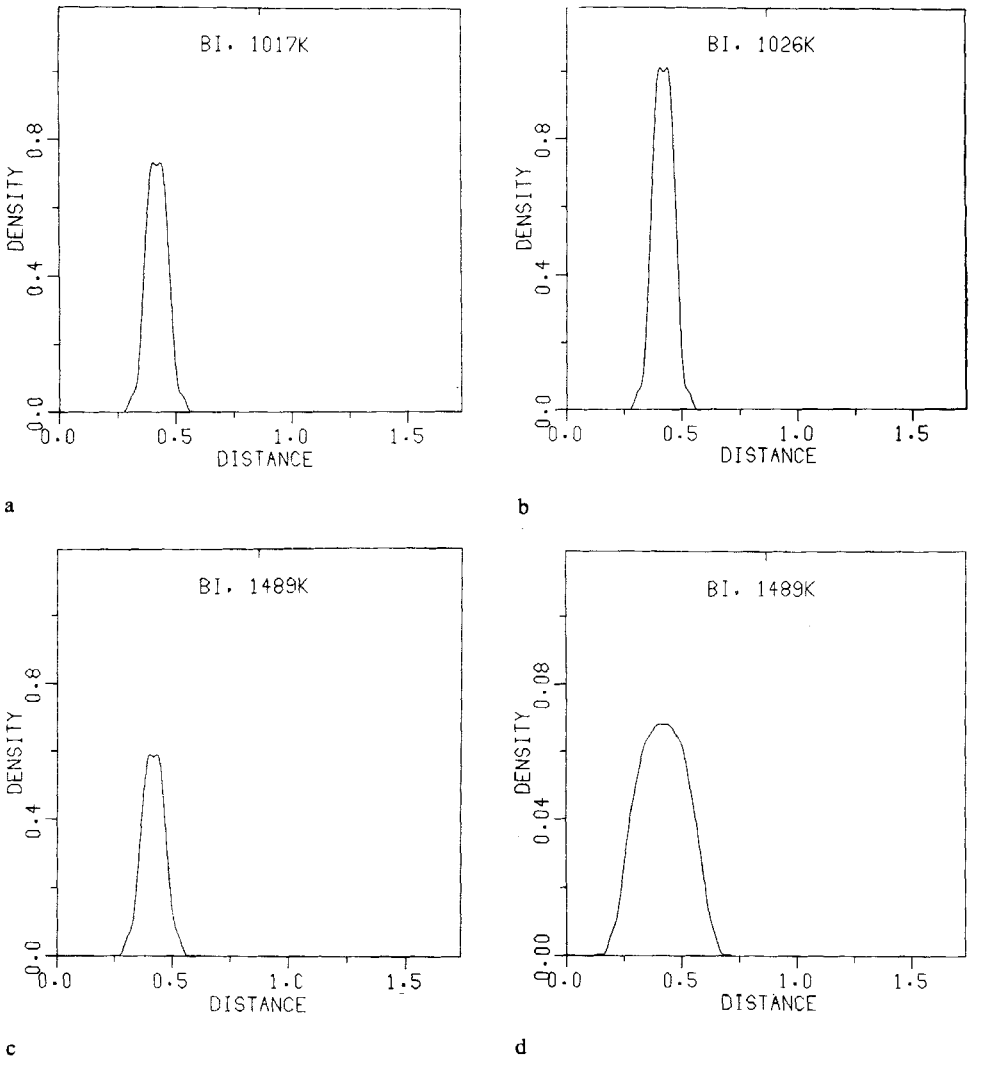

Figure 8 Bi^{3+} density along $<111>$. Units as in Figure 6 but with a grid element size of $\sqrt{3}a/32$.

Averaging of the (100) and (200) planes does not eliminate these features (Figure 11f). Details of the statistical treatment of the data are given in the appendix.

O^{2-} densities in the (110) plane are a little more difficult to interpret. The quartet structure in the central peak (Figures 12d, 12e) would appear to be caused by $<111>$ O^{2-} displacements. The doublet structure evident at the plot corners (Figure 12e) could be the result of either $<100>$ or $<110>$ displaced O^{2-}'s. In brief, the 3-*D* density plots (Figures 11,12) show clear evidence of displacements of O^{2-}'s from their lattice sites along $<100>$ and $<111>$ directions with possible evidence of displacement along $<110>$ directions.

Interpretation of these features in the O^{2-} density distribution is facilitated by plots

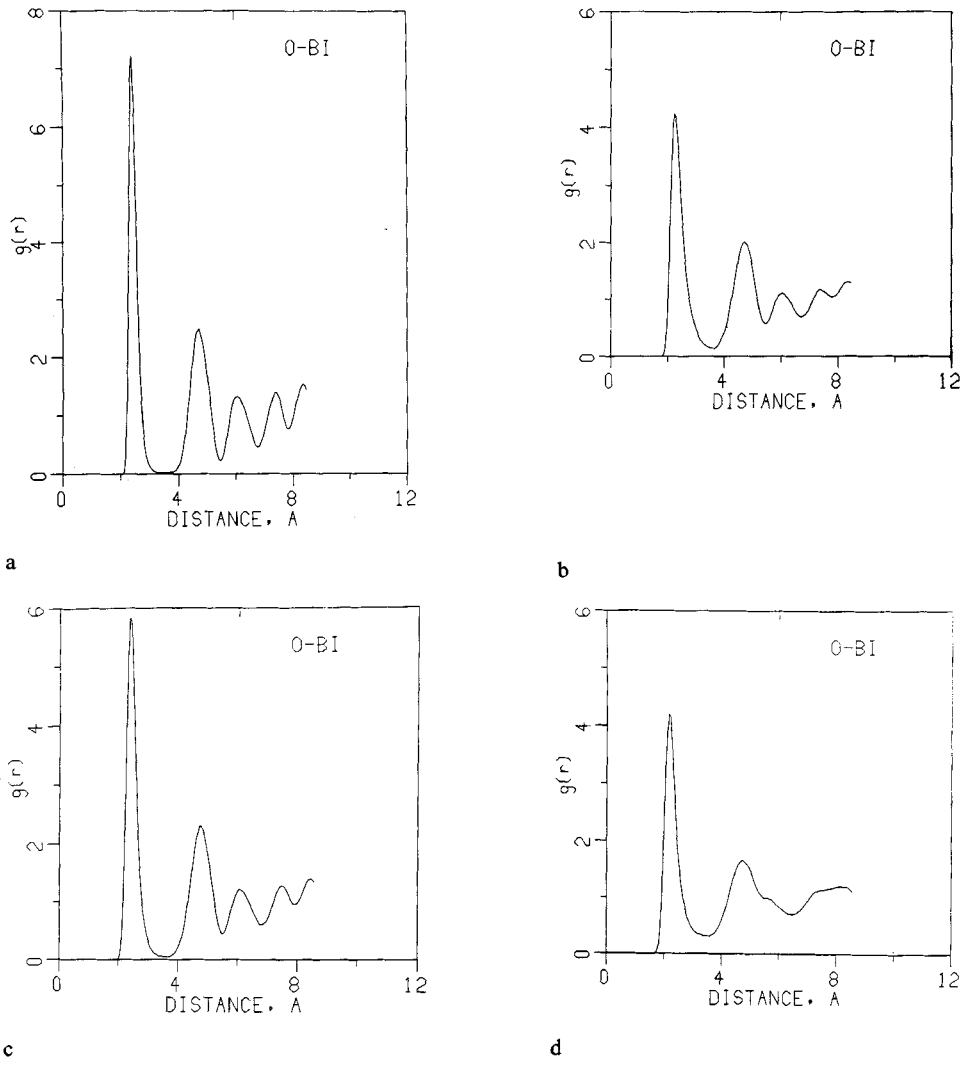

Figure 9 O^{2-}-Bi^{3+} radial distribution function $g(r)$ as a function of distance r in Å.

of O^{2-} density along the principal directions in the cubic δ-Bi_2O_3 lattice shown in Figures 13–15. The broadening in the O^{2-} density distribution brought about by dielectric adjustment of the potential (Figures 13b, 14b, 15b), the marked decrease in the peak O^{2-} density by a factor of 10 for II-*D*2-2 (Figures 13d, 14d, 15d) compared to II-*R*2-2 (under the same relaxed conditions, Figures 13c, 14c, 15c), the non-zero O^{2-} density along <100> but not <110> or <111> (contrast Figures 13d with 14d and 15d) and the structure in the O^{2-} peak for II-*D*2-2 (Figures 13d, 14d, 15d), are all seen clearly. While the O^{2-} density along <110> merely appears broadened (Figure 14d), there is a double maximum evident along <100> (Figure 13d) and another, more intense doublet along <111> directions (central peak), occurring

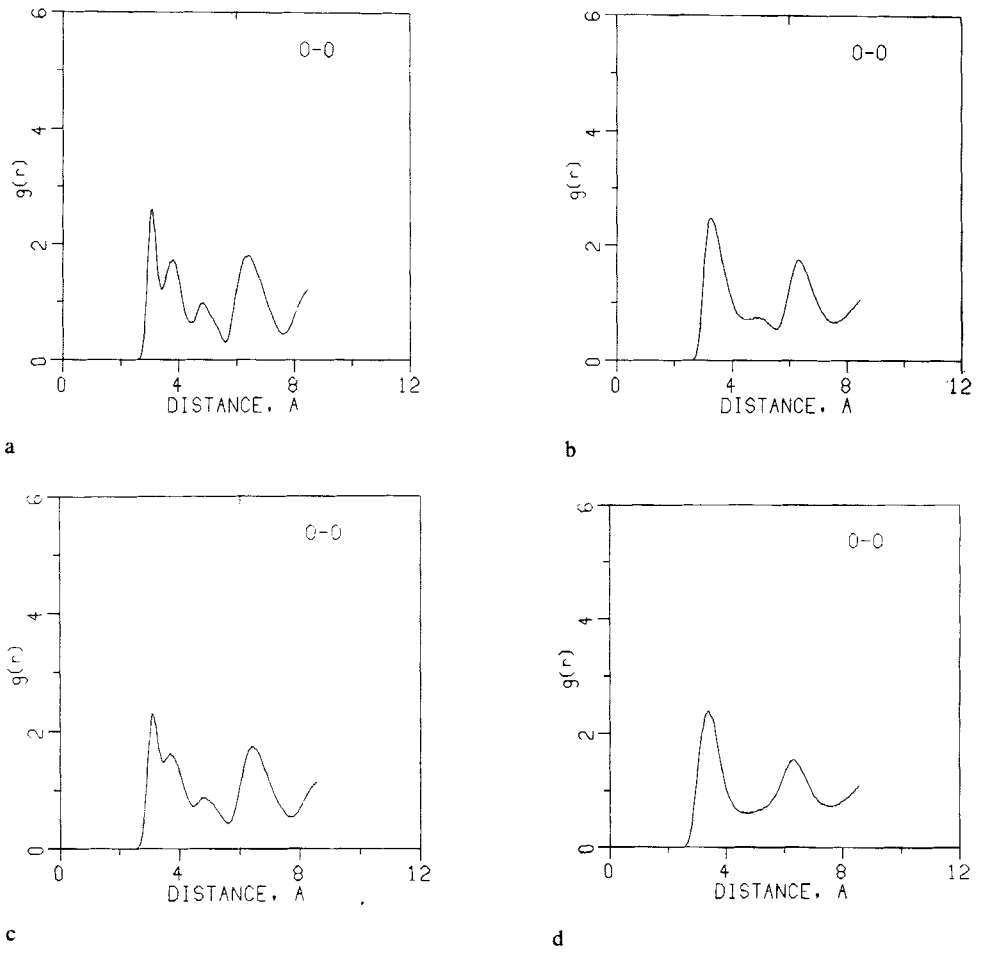

Figure 10 O^{2-}-O^{2-} radial distribution function $g(r)$ as a function of distance r in Å.

again as shoulders in edge peaks (Figure 15d, Table 2). This double maximum along $<111>$ is reminiscent of Willis disorder [5,6] a point which we return to below. Both the 3-D and line density plots show clear evidence of O^{2-} displacement along $<100>$ directions. Other displacements evident in the 3-D plots are shown clearly by the line density plots to be due to $<111>$ displacements, a widely observed feature of fluorites [5–8]. Thus we have clear evidence of both $<100>$ and $<111>$ displacements but no unambiguous evidence for $<110>$ displacements. As shall be seen below, these results are in excellent agreement with the results of diffraction studies.

It should be emphasized that the density plots along specific directions were averaged over all equivalent directions in all 27 unit cells of the simulation box. The O^{2-} atom at $\sqrt{n}a/2$ was further assumed to be on a plane of symmetry normal to the specific direction, with $n = 1, 2, 3$ respectively in Figures 13, 14, 15, but no averaging was done of the O^{2-} atom density over the equivalent sites at $\sqrt{n}a/2$ and at $0\ (=\sqrt{n}a)$. This is consistent with lattice basis vectors of length a, but not of length $a/2$.

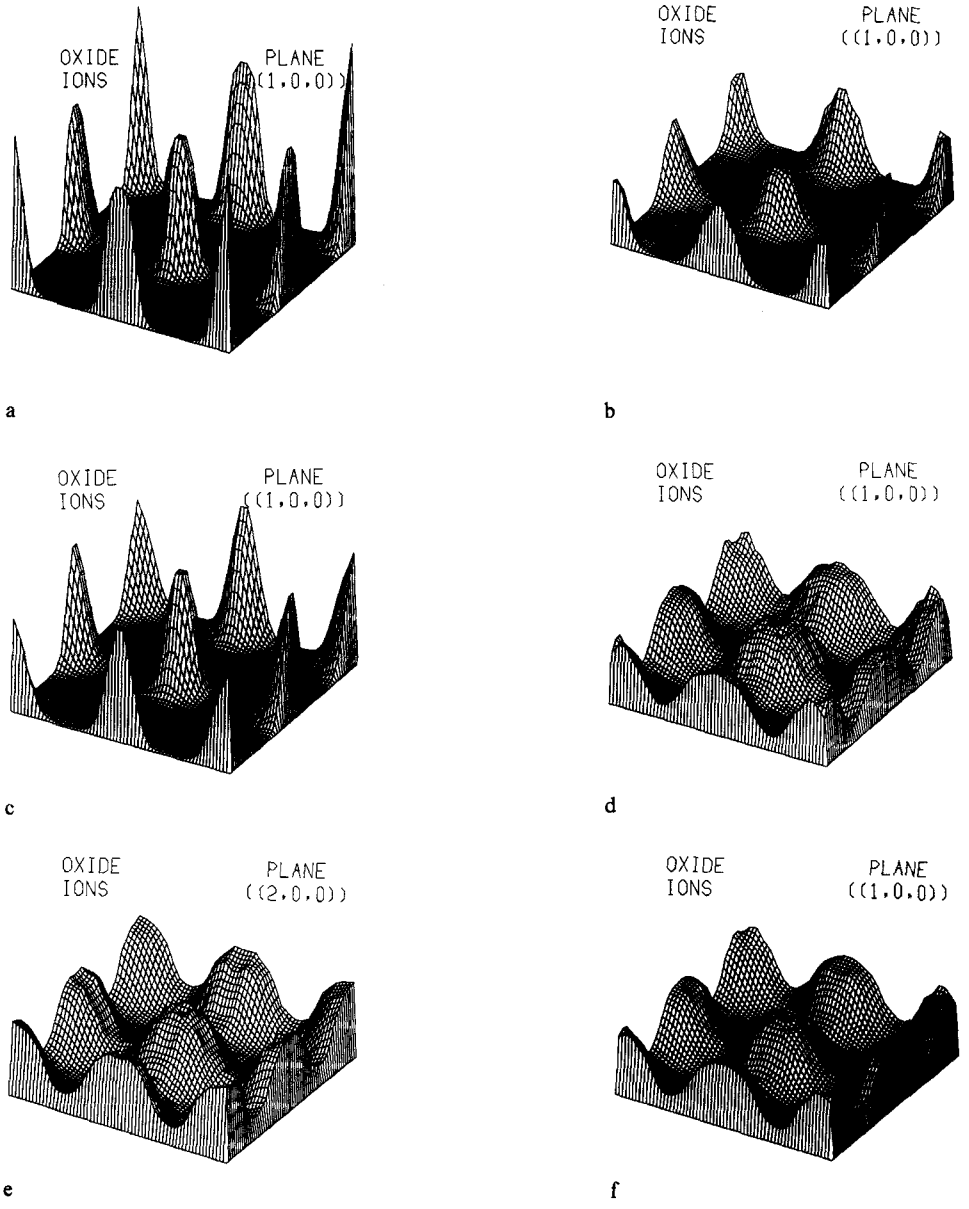

Figure 11 (a)-(d) O^{2-} density in the (100) plane (a)-(d), having their usual connotations (Table 1). In (d), II-*D*2-2, the O^{2-} density is multiplied by a factor of four compared with (a), (b) and (c). (e) shows the O^{2-} density in the equivalent (200) plane is on the same scale as Figure 11d. (f) shows the average of the (100) and (200) planes (simulation II-*D*2-2).

3.1 Oxygen Migration

O^{2-} migration is observed in all four simulations but is greatest in II-*D*2-2. In all four runs O^{2-} migration is along cube edges. Some jumps occur directly between lattice

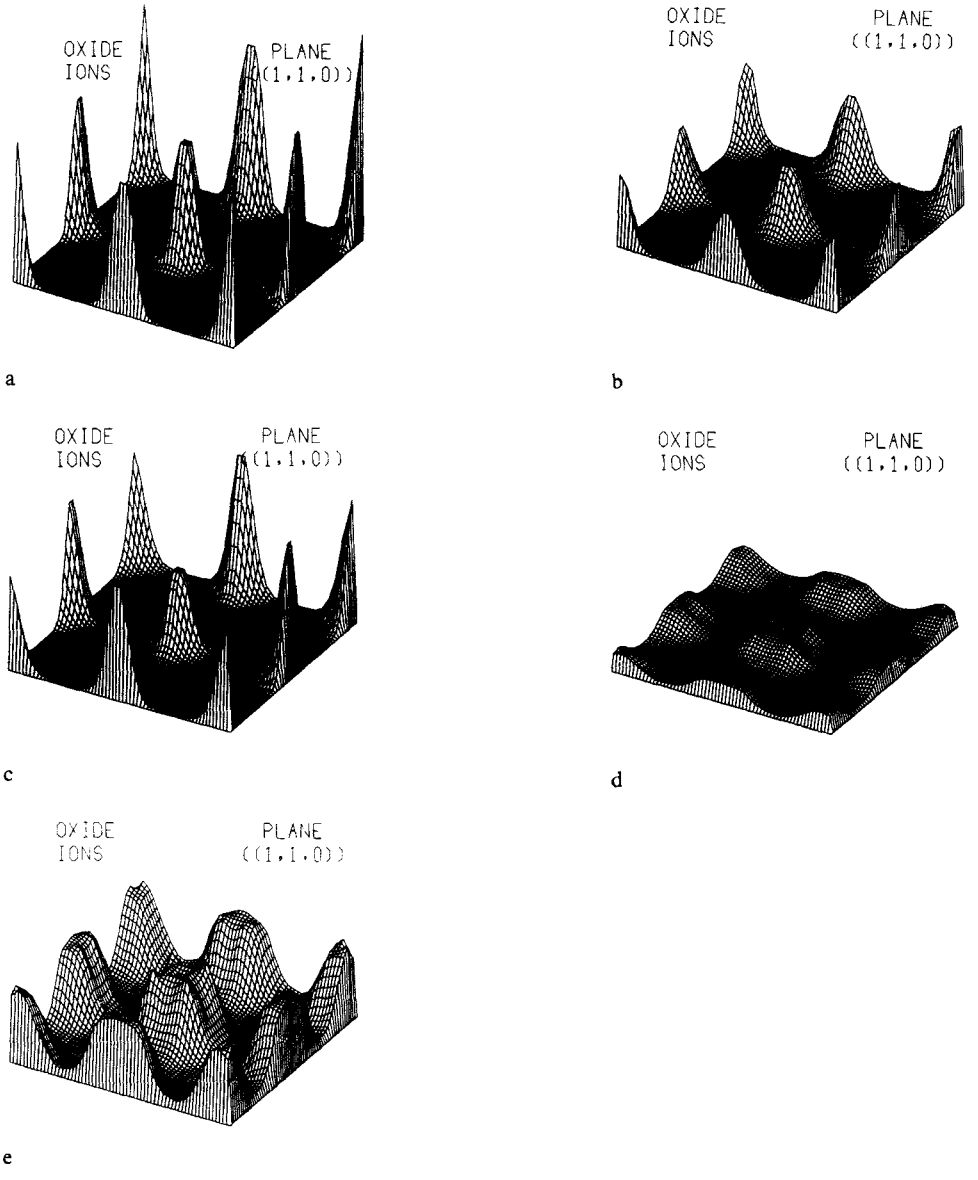

Figure 12 (a)-(d) O^{2-} density in the (110) plane, (a)-(d) having their usual connotation. (e) shows the O^{2-} density in (110) multiplied by a factor of four compared to Figure 12d. The central peak particularly now shows very clearly the fine structure due to $<111>$ O^{2-} displacements.

sites but others occur via interstitials half-way along a cube edge. Both these migration patterns may be observed clearly in trajectory plots [1]. The number of interstitials is small and so they cannot be resolved in the plots of O^{2-} density in the (100) or (110) planes (Figures 11,12). However, there is significant O^{2-} density in the (400) Bi^{3+} plane (Figure 16a), half-way between (100) O^{2-} planes. Because the population

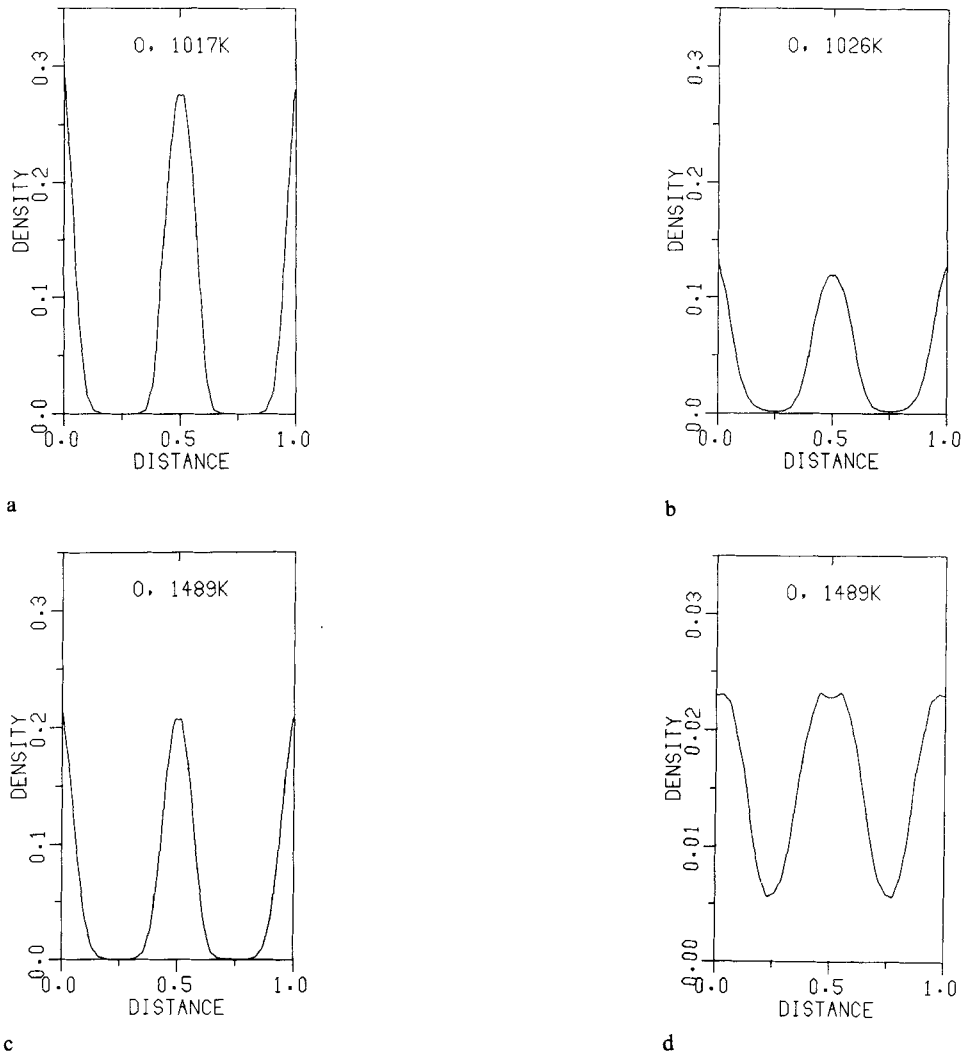

Figure 13 O^{2-} density along $<100>$. Units and grid element size as in Figure 6.

of cube-edge interstitials is small the statistics are poor and it was necessary to make extensive use of lattice symmetry. Consequently, any evidence of the interstitials being displaced from the cube-edge is lost. However, examination of the unsymmetrized O^{2-} density in the (400) plane suggests that the O^{2-} density is displaced slightly from the $<100>$ cube edge (along $<110>$ directions) towards a vacant cube centre (cf. the Bi^{3+} positions in the same plane in Figure 4d). Unfortunately, the statistical fluctuations are large and the results are inconclusive. Trajectory analysis of the migrating O^{2-}'s (Figure 6 in ref. [1]) is also inconclusive on this point. Static lattice calculations however, do predict $<110>$ displacements [3] in close agreement with those found experimentally [7,8].

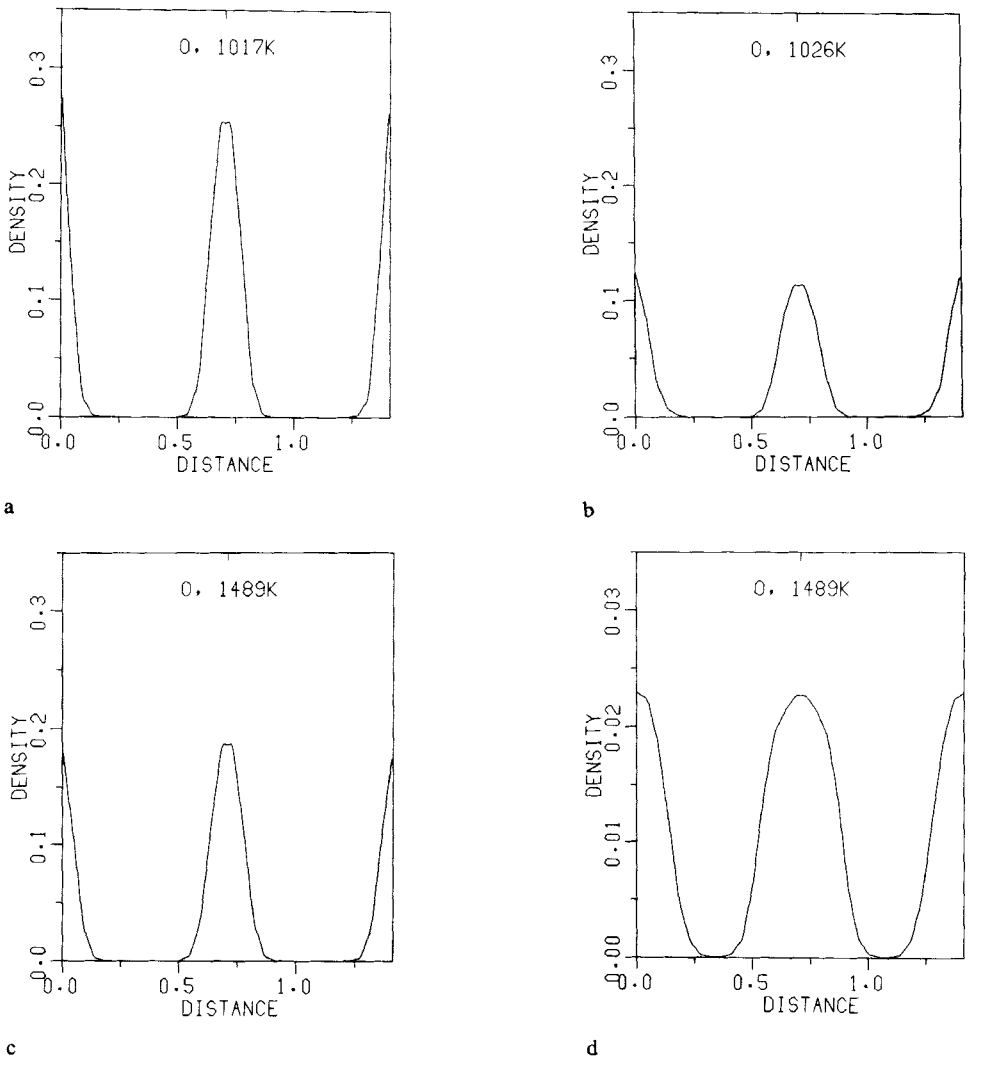

Figure 14 O^{2-} density along <110>. Units as in Figure 6 and grid element size as in Figure 7.

3.2 Willis Disorder

In simulation II-*D*2-2 the structure in the O^{2-} density distribution in Figures 13, 14, 15 is most marked along <111> (Figure 15d, Table 2). This is consistent with Willis disorder [5] in fluorite structures, in which anions undergo <111> displacements towards the corners of a tetrahedron. Willis displacements should show up as slight maxima along <110> directions in (100) planes and as slightly greater maxima along the plot diagonals in (110) planes. This is precisely what is observed. In the (110) plane depicted in Figures 12d, 12e the displaced maxima are clearly seen (central peak), and the resemblance of the multiplet structure to the fourier difference map for the O^{2-}

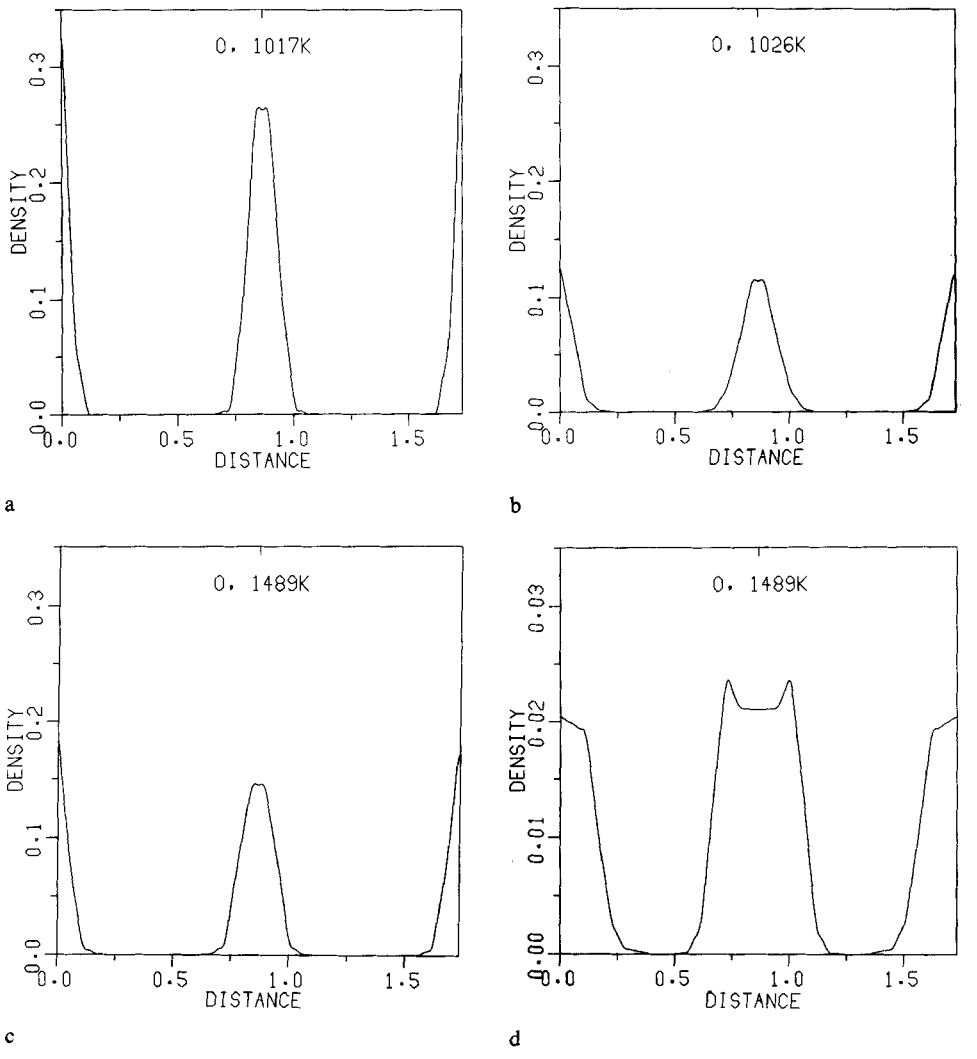

Figure 15 O^{2-} density along $<111>$. Units as in Figure 6 and grid element size as in Figure 8.

sublattice in pure Bi_2O_3 [7] is striking. The strength of these maxima are such that they are unlikely to be due to statistical noise. Examination of the (200) O^{2-} plane in Figure 11e shows shoulders along $<110>$ directions in the O^{2-} peaks at the $a/2$ positions half-way along cube edges. However, there are also maxima along $<100>$ directions; these are particularly evident in the central O^{2-} peak, although they are not as marked as those due to $<111>$ displaced O^{2-}'s seen in the (110) plane. Evidence for $<100>$ displacements is more clearly seen in Figures 11d, 11e. Thus MD simulation provides clear evidence of both $<100>$ and $<111>$ O^{2-} displacements in δ-Bi_2O_3 although $<110>$ displacements cannot be ruled out. It is of note that in a recent neutron diffraction study on $(Bi_2O_3)_{0.75}(Y_2O_3)_{0.25}$ O^{2-} displacements along both $<100>$ and $<111>$ directions are reported [9].

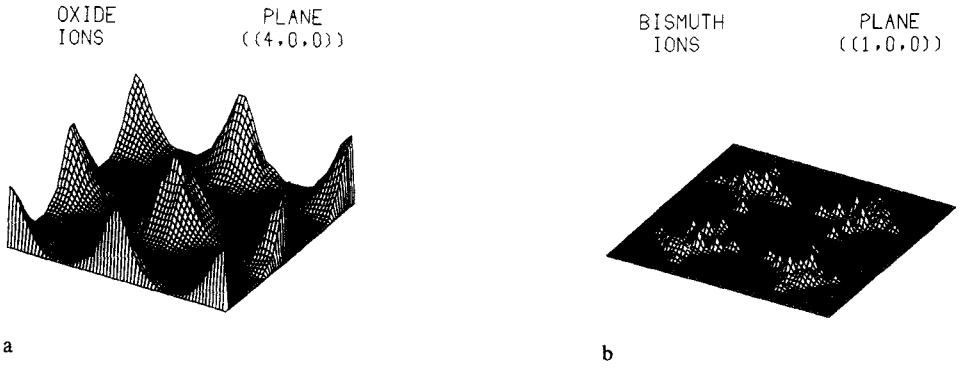

Figure 16 (a) O^{2-} density in the (400) Bi^{3+} plane. The oxygen density maxima lie at cube-edge interstitial sites. By comparsion with Figures 11 and 12 the scale of this figure has been magnified twenty times. (b) Bi^{3+} density in the (100) O^{2-} plane, same scale as in (a).

4. DISCUSSION

It is quite clear from the four simulations described that both dielectric adjustment and relaxed conditions are required if fast-ion conduction is to be observed. Adjustment of the *nn* (Bi^{3+}-O^{2-}) potential to re-fit the static dielectric constant is usually considered advisable in both static and dynamic computer simulation studies when a fitted shell-model potential is changed to a rigid-ion potential. Relaxed conditions often seem to be necessary in MD simulations to compensate approximately for constant-volume conditions that discourage melting, for example [2]. The Bi^{3+} sub-lattice remained highly structured unless both these conditions were met. When both were applied however, the Bi^{3+} density maximum in the (400) plane fell by an order of magnitude and the vibrational amplitude of Bi^{3+} ions increased to such an extent that occasionally Bi^{3+} vibrations penetrated the surrounding O^{2-} cubic-cage, as seen in the non-zero Bi^{3+} density in the O^{2-} (100) plane for II-*D*2-2 (Figure 16b). Whether such a large vibrational amplitude is a necessary requirement for fast-ion conduction or simply a consequence of it, or indeed a feature of this simulation alone, we have not as yet determined. It should be noted, however, that during an O^{2-} $<100>$ vacancy jump (along a cube-edge), the migrating O^{2-} must pass between two Bi^{3+} ions (positioned along $<110>$ directions) at the energy maximum. Large vibrational amplitudes in the Bi^{3+} sub-lattice, if correlated such that the Bi^{3+} to migrating O^{2-} distance is increased, will tend to minimize the resistance to O^{2-} motion. If this is so one might expect to calculate a lower activation energy for O^{2-} migration in an MD simulation than in a static lattice calculation [3] where the ions relax in the saddle point but are not vibrating. We return to this point in a subsequent paper (Part III, [10]) in which we analyze various dynamic effects, including the velocity autocorrelation function and the calculated diffusion coefficients. It may well be, however, that the enhanced O^{2-} mobility and the increased amplitude of the Bi^{3+} vibrations observed in II-*D*2 are both consequences, essentially independent, of the adjustment to the potential, lattice expansion and increased temperature, with the greater vibrations of the Bi^{3+} sub-lattice mainly a consequence of the increased space available and of the increased kinetic energy. This effect would be enhanced by its interactions with a rapidly changing O^{2+} sub-lattice environment.

In a study on $(Bi_2O_3)_{1-x}(Y_2O_3)_x$ Battle *et al.* [7,8] report $<100>$ Bi^{3+} displace-

ments which Moroney [11] has suggested might be correlated with $<110>$ vacancy ordering. In static lattice simulations using potential set *R*1, such a correlation was indeed observed [3] but with the same potential in simulation I-*R*1, significant Bi^{3+} displacements are found, but not particularly along $<100>$ directions (Figures 3a, 4a). When fast-ion conduction is achieved (simulation II-*D*2-2) the amplitude of Bi^{3+} vibrations is significantly enhanced (Figures 3d, 4d) but 3-D density plots (Figure 4d) do not suggest that $<100>$ directions are particularly favoured. Examination of the line densities along the three principle directions (Figures 6, 7, 8) yield little further detail about the behaviour of the Bi^{3+} sub-lattice.

In a recent neutron diffraction study of $(Bi_2O_3)_{1-x}(Y_2O_3)_x$, with $x = 0.25$, Infante *et al.* [9] reported $<111>$ rather than the $<100>$ cation displacements observed by Battle *et al.* [7,8] for similar systems. Thus there is apparently some disagreement in the interpretation of the experimental diffraction data for the Y^{3+} doped Bi_2O_3. δ-Bi_2O_3 and its doped analogues are notoriously difficult to refine and many structures have been proposed. It may be that there are two candidate structures and that the currently available experimental data is unable to distinguish between them. Alternatively there may genuinely exist, two or more fluorite structures. Indeed, there is some experimental evidence which lends weight to such an explanation. Tsubaki and Koto [12] point out that the temperature of transition and the appearance of metastable forms is influenced by the rate of cooling of the δ-phase and the maximum temperature achieved. For example, metastable forms (the β- and γ-phases) do not form if the sample has been heated above 1163 K, which is well above the melting point. This strongly suggests that the δ-phase 'remembers' its history. The Bi^{3+} sub-lattice has a well defined fcc structure, but the O^{2-} sub-lattice is notoriously difficult to determine, with most authors reporting different structures (*cf.* [3] and references therein). Such a memory might, therefore, be expressed as configurational order in the O^{2-} sub-lattice. Some doped Bi_2O_3 systems undergo anamalous expansions, while retaining the fluorite structure [13, 14]. This also suggests a change in the structure of the O^{2-} sub-lattice since the cation sub-lattice is found to retain the fcc structure. Application of Vegard's rule to fluorite solid solutions with Bi_2O_3 at room temperature suggest that Bi_2O_3 and the rare-earth sesquioxides have a minimum of two fluorite forms, differing only in O^{2-} sub-lattice structure [4]. (The fluorite forms for the rare-earth sesquioxides are of course only stable in solid solution and are not found in the pure form).

One might suppose that Bi^{3+} displacements occur in response to the structure of the O^{2-} sub-lattice environment. Battle *et al.* [7,8] report $<100>$ Bi^{3+} displacements in Y_2O_3 doped Bi_2O_3 while Infante *et al.* [9] report $<111>$ displacements. This also may be evidence of different O^{2-} sub-lattices. However, Battle *et al.* reported no $<100>$ Bi^{3+} displacements for undoped Bi_2O_3 [8], nor were such displacements observed in simulation II-*D*2-2. It would, therefore, appear that Bi^{3+} displacements are only to be found in the heavily doped Bi_2O_3 or with $<110>$ vacancy ordering [3].

Finally, we should note that Bi^{3+} has a polarizable 6*s* shell and that the ion is consequently liable to deform in response to the configuration of the O^{2-} vacancies around it. Such distortions would encourage anisotropic vibrations and possibly cause atom displacements along some preferred direction. Our MD model is that of an unpolarizable Bi^{3+} ion which would not therefore reflect behaviour depending on cation polarization. However, the Bi^{3+} density in the (400) plane (Figure 4d) does show some structure, which may possible be related to slight Bi^{3+} displacements along $<111>$.

The O^{2-} sub-lattice results are more detailed and interesting. Most diffraction studies [7,8,9,15] have reported small <111> Willis-like displacements. Battle *et al.* [7,8] report 43% of the O^{2-} density on 32*f*; (x,x,x); $x = 1/4 + \delta$ (Willis <111>) sites and 57% on the normal fluorite 8*c*; (1/4, 1/4, 1/4) lattice sites ((0, 0, 0) in Figure 1) for pure Bi_2O_3 at 1023 K. (Coordinates refer to the usual crystallographic unit cell comprising a fcc arrangement of Bi^{3+} ions.) From their data a value for the displacement of 1.02 Å can be calculated (Table 2). For $(Bi_2O_3)_{1-x}(Y_2O_3)_x$ at 1023 K, with $x = 0.27$, 61% are on fluorite 8*c* lattice sites, 33% on 32*f*; (x,x,x) sites (displacement = 0.68 Å) and 5% on 48i; $(1/2,v,v)$ cube-edge interstitial sites. Room temperature diffraction results differ little with a <111> displacement of 0.65 Å. By contrast, Infante *et al.* [9] in their room temperature study of Y_2O_3 doped Bi_2O_3 ($x = 0.25$) report zero density on fluorite lattice sites, 78% on 48g; $(1/4 + v, 1/4, 1/4)$ sites (relaxed along <100> from ideal 8*c* sites) and 22% on 32*f* Willis sites. In the latter room temperature study the Willis (32*f*) sites are removed from the regular lattice (8*c*) sites by 0.80 Å. Simulation II-*D*2-2 predicts a comparable value of 0.77 ± 0.15 Å (Table 2), close to that of Infante *et al.* [9]. Moreover, the <100> O^{2-} displacement of 0.335 Å observed by Infante *et al.* [9] is in excellent agreement with simulation II-*D*2-2 which predicts a value of 0.27 +/− 0.09 Å (Table 2). This feature was not reported by Battle *et al.* [7,8]. The location of the maxima in the O^{2-} density at ideal lattice sites has the quartet structure characteristic of Willis disorder (Figure 12e).

Cube-edge interstitials mark the mid-point of O^{2-} vacancy migration. Battle *et al.* [7,8] did not observe any cube-edge interstitials for pure Bi_2O_3. However, an approximately 5% concentration is found in Y_2O_3 doped Bi_2O_3 with $x = 0.27$ [8], although Infante *et al.* [9] did not include these interstitials in their analysis. In our fast-ion simulation the concentration of these interstitials is small and therefore not resolvable in O^{2-} density plots for the (100) plane which may explain why they were not observed experimentally for pure δ-Bi_2O_3. They can be seen, however, in the Bi^{3+} (400) plane half-way along a cube-edge and displaced slightly towards vacant cube centres, i.e. at 48*i*; $(1/2,v,v)$ crystallographic sites, exactly as found in $(Bi_2O_3)_{1-x}(Y_2O_3)_x$ with $x = 0.27$ [7,8] (Figure 16a). Static lattice calculations [3] also predicted these interstitials but only in the presence of complex <110> vacancy clusters with a net excess of vacancies, thus indicating the presence of transiently ordered, complex arrangements of O^{2-} vacancies even at high temperatures. Our fast-ion simulation results for the O^{2-} sub-lattice (II-*D*2-2) have features characteristic of both models.

5. CONCLUSION

MD simulations of δ-Bi_2O_3 show substantial structure in the 'liquid' O^{2-} sub-lattice. Significant O^{2-} densities are observed at sites displaced along both <100> and <111> directions, in addition to the normal cubic sites which retain much density. $O^{2-}s$ are also observed half-way along cube-edges, corresponding to the mid-way position of an O^{2-}-vacancy migration. The simulations suggest a structure intermediate between two different models, both based on experimental diffraction data. It is suggested that there exist, not one, but two or more fluorite phases, differeing in the O^{2-} sub-lattice structure.

One of the main results of this paper is the structure seen in the peaks of O^{2-} density (Figures 11–15). The precise symmetry, but not the existence, of this structure is a

consequence of the symmetrization used in evaluating the O^{2-} density, and which is essential in order to get satisfactory statistics. Otherwise nothing useful could be deduced from density maps. The only way to avoid symmetrization is to use a larger system that will permit averaging the densities over a large number of unit cells. We hope to report results for larger systems at some future date.

Acknowledgement

This research was supported by the Natural Sciences and Engineering Research Council of Canada.

APPENDIX

The statistical treatment of the data presented in this work varies slightly from case to case and so some clarification is warranted. The data for the radial distribution functions (RDF's) was not collected over the whole simulation but over the last 500 time steps. This proved more than adequate as RDF's converge rapidly with time, provided that all particles are considered.

Density distributions within the unit caell were collected in a 3-D 32 × 32 × 32 grid, which is the maximum power of 2 size that can be used on the Cyber 180/835 because of memory limitations. Choosing a power of 2 grid size enables the further elaboration of these data by the power of 2 FFT, which we use for the calculation of, for example, $S(q)$.

The 3-D density plots, such as those of the (400) and (220) planes (Figures 4 and 5) are based on a 32 × 32 grid. This is extended to a 64 × 64 grid by means of linear interpolation followed by smoothing in Fourier space. The square grid is retained regardless of the plane in question. The lattice constant in II-*D*2-2, for example, is 5.721 Å and thus the (100) plane has a resolution of 0.179 Å in the x and y directions, whereas the (110) plane, while retaining a resolution of 0.179 Å along <100> directions, has a resolution of only 0.253 Å along <110> directions.

Averaging was performed over all 27 cells in the simulation box. Bi peaks are quite large with a large signal to noise ratio and it is not necessary to make use of any higher symmetry within the lattice. By contrast, O density peaks are broader and smaller, yielding a significantly smaller signal to noise ratio. Accordingly full use of cell symmetry was made in order to improve the quality of the data. However, this did not inlcude averaging over equivalent sites separated by distances less than a. Full use of cell symmetry was also made for similar reasons in the plots of O density in the Bi (400) plane and Bi density in the O (100) plane as the densities in these cases are very small.

Line density plots (Figures 6, 7, 8, 13, 14, 15) were all based on a 32 element grid. This was extended to 2000 points by linear interpolation and followed by Fourier smoothing. The resolution is 0.179 Å, 0.253 Å and 0.310 Å along the <100>, <110> and <111> directions, respectively. This limiting resolution is the source of the estimated error in the calculated displacements along <100> and <111> directions (Table 2).

References

[1] D.A. Mac Dónaill, P.W.M. Jacobs and Z.A. Rycerz, "Molecular dynamics simulation of the fast ion conductor δ-Bi_2O_3.", *Molecular Simulation*, *3*, 155 (1989).

[2] J. Móscinski and P.W.M. Jacobs, "Computer simulation of defect motion in model normal and 'fast ion' conductors. II. $SrCl_2$", *Proc. Roy. Soc. A.*, **398**, 173 (1985).
[3] P.W.M. Jacobs and D.A. Mac Dónaill, "Computational simulations of δ-Bi_2O_3", *Parts I, II and III, Solid State Ionics*, **23**, 279, 295, 307 (1987).
[4] D.A. Mac Dónaill and P.W.M. Jacobs, "On the lattice parameter of some oxides with the fluorite structure", *J. Solid State Chem.*, **84** in the press.
[5] B.T.M. Willis, "The anomalous behaviour of the neutron reflexions in fluorite", *Acta. Cryst.*, **18**, 75 (1965).
[6] B.T.M. Willis, "Neutron diffraction studies of the actinide oxides, I. uranium dioxide and thorium dioxide at room temperature", *Proc. Roy. Soc., A* **274**, 122 (1963).
[7] P.D. Battle, C.R.A. Catlow, J. Drennan and A.D. Murray, "The structure properties of the oxygen conducting δ-phase of Bi_2O_3", *J. Phys., C* **16**, L561 (1983).
[8] P.D. Battle, C.R.A. Catlow, J.W. Heap and L.M. Moroney, "Strucural and dynamical studies of δ-Bi_2O_3 oxide ion conductors. I. The structure of $(Bi_2O_3)_{1-x}(Y_2O_3)$ as a function of x and temperature", *J. Solid State Chem.*, **63**, 8 (1986).
[9] C.E. Infante, C. Gronemeyer and F. Li, "Neutron diffraction study of the oxide conducting δ-phase of $(Bi_2O_3)_{1-x}(Y_2O_3)_x$ ($x = 0.25$)", *Solid State Ionics*, **25**, 63 (1987).
[10] D.A. Mac Dónaill and P.W.M. Jacobs, "Molecular dynamics simulation of the fast ion conductor δ-Bi_2O_3. III. dynamic structure", *Molecular Simulation*, **5**, 215–231 (1990).
[11] L.M. Moroney, private communication.
[12] M. Tusbaki and K. Koto, , "Superstructures and phase transitions of Bi_2O_3", *Mat. Res. Bull.*, **19**, 1613 (1984).
[13] M.J. Verkerk, G.M.H. van de Velde, A.J. Burggraaf and R.B. Helmholdt, "Structure and ionic conductivity of Bi_2O_3 substituted with lanthanide oxides", *J. Phys. Chem. Solids*, **43**, 1129 (1982).
[14] M.J. Verkerk, K. Keizer and A.J. Burggraaf, "High oxygen ion conduction in sintered oxides of the Bi_2O_3-Er_2O_3 system", *J. Appl. Electrochem.*, **10**, 81 (1980).
[15] K. Koto, H. Mori and Y. Ito, "Oxygen disorder in fluorite-type conductors $(Bi_2O_3)_{1-x}(Gd_2O_3)_x$ by X-ray and EXAFS analyses", *Solid State Ionics*, **18/19**, 720 (1986).